iScience

CellPress
OPEN ACCESS

Article

Regulation of Ce (III) / Ce (IV) ratio of cerium oxide for antibacterial application

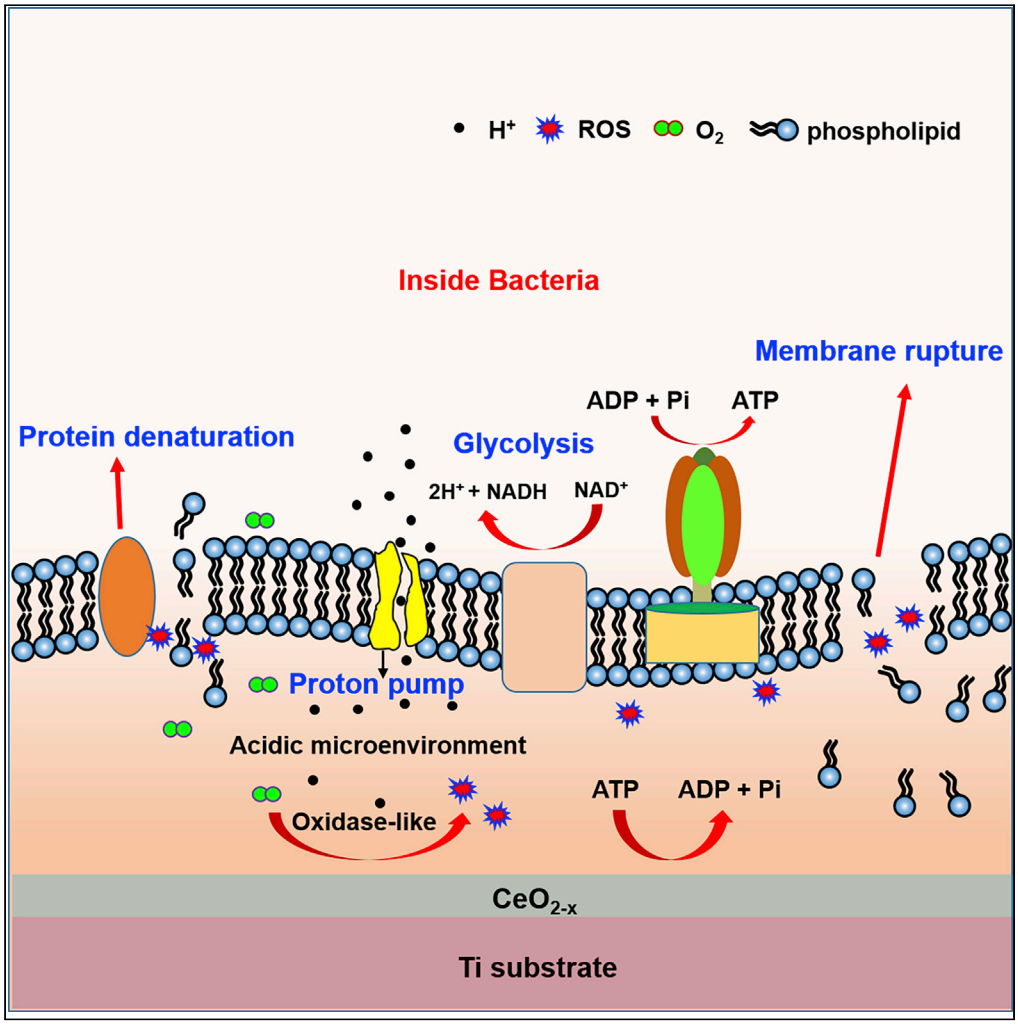

Haifeng Zhang, Jiajun Qiu, Bangcheng Yan, Lidan Liu, Dafu Chen, Xuanyong Liu

chendafujst@126.com (D.C.)
xyliu@mail.sic.ac.cn (X.L.)

HIGHLIGHTS

Cerium oxide films were fabricated on the titanium surface by pyrolysis of Ce-BTC

The valence states of cerium element on cerium oxide can be modulated flexibly

CeO_{2-X} with high Ce (III)/Ce (IV) ratio possessed high antibacterial rate

Antibacterial rate is related to the oxidase-like and ATP deprivation capacity

Zhang et al., iScience 24, 102226
March 19, 2021
https://doi.org/10.1016/j.isci.2021.102226

iScience

CellPress
OPEN ACCESS

Article

Regulation of Ce (III) / Ce (IV) ratio of cerium oxide for antibacterial application

Haifeng Zhang,[1,3,5] Jiajun Qiu,[1,5] Bangcheng Yan,[1,3] Lidan Liu,[1,3] Dafu Chen,[2,6,*] and Xuanyong Liu[1,3,4,6,*]

SUMMARY

Antibiotics have been considered as effective weapons against bacterial infections since they were discovered. However, antibiotic resistance caused by overuse and abuse of antibiotics is an emerging public health threat nowadays. Fully defeating bacterial infections has become a tough challenge. In this work, cerium oxide was fabricated on medical titanium by thermolysis of cerium-containing metal-organic framework (Ce-BTC). Regulation of Ce (III)/Ce (IV) ratios was realized by pyrolysis of Ce-BTC in different gas environment, and the antibacterial properties were studied. The results indicated that, in acidic conditions, ceria with a high Ce (III)/Ce (IV) ratio owned high oxidase-like activity which could produce reactive oxygen species. Moreover, ceria with high Ce (III) content possessed strong ATP deprivation capacity which could cut off the energy supply of bacteria. Based on this, ceria with a high Ce (III)/Ce (IV) ratio exhibited superior antibacterial activity

INTRODUCTION

There is no doubt that antibiotics are the most successful drugs developed over the past few centuries which not only save countless lives but also enable modern medical procedures (Wright, 2011). Unfortunately, due to the abuse of antibiotics, antibiotic resistance has become an emerging public health threat where antibacterial resistance brings about 700,000 deaths per year and the number of deaths will keep rising unless actions are taken. Fully defeating bacterial infections has become a tough challenge in various fields including biomedical implants and devices (Chen et al., 2018).

To address this problem, many works have been done to develop alternative antibacterial materials. For instance, metal or metal oxide nanoparticles such as Cu, Ag, and ZnO are used (Cao et al., 2018b; Li et al., 2016, 2019a; Sirelkhatim et al., 2015; Xia et al., 2020; Yang et al., 2020). Nevertheless, the dose-dependent cytotoxicity limits their applications. Currently, cerium oxide has attracted increasing attention for biological applications due to its catalytic activity which derives from the reversible switch between redox pairs Ce (III)/Ce (IV) (Li et al., 2019b). In general, the catalytic activity of cerium oxide is closely related to the content of Ce (III) and oxygen vacancies (Dong and Huang, 2019). Cerium oxide with a high content of Ce (III) usually has abundant oxygen vacancies which are beneficial to easier oxygen exchange and redox reactions (Cao et al., 2018a). At basic physicochemical pH, Ce (III)/Ce (IV) couple exhibits antioxidant properties by scavenging reactive oxygen species (ROS). At acidic pH, the Ce (III)/Ce (IV) couple shows prooxidant properties by producing ROS (Mehmood et al., 2018). This unique redox potential of cerium oxide can be used to provide protection for normal cells and exhibit cytotoxic effects for bacteria in an acidic environment. Moreover, lanthanide-based materials such as cerium oxide usually possess high deprivation capacity toward ATP and cause cell death by cutting off the energy supply (Cao et al., 2018a).

Based on the high oxidase-like activity and ATP deprivation ability, cerium oxide may show tremendous potential for antibacterial applications in the field of biomedical implants and devices. Many methods have been used to construct cerium oxide coatings on implant surface with different Ce (III)/Ce (IV) ratio, such as plasma sprayed (Shao et al., 2020), magnetron sputtering (Hu et al., 2018), and atomic layer deposition (Gupta et al., 2019), but cerium oxides in these coatings tend to exist in aggregated states with limited catalytic activity. Currently, porous metal oxides derived from metal-organic frameworks (MOFs) with high surface areas and tunable porosity have been widely utilized as high-performance catalysts (Li et al., 2015). Moreover, the porous carbonaceous structures which transformed from organic linkers of MOFs during thermolysis process in inert atmosphere can avoid the potential aggregation from metal

[1]State Key Laboratory of High Performance Ceramics and Superfine Microstructure, Shanghai Institute of Ceramics, Chinese Academy of Sciences, Shanghai 200050, China

[2]Laboratory of Bone Tissue Engineering, Beijing Laboratory of Biomedical Materials, Beijing Research Institute of Orthopaedics and Traumatology, Beijing JiShuiTan Hospital, Beijing 100035, China

[3]Center of Materials Science and Optoelectronics Engineering, University of Chinese Academy of Sciences, Beijing 100049, China

[4]School of Chemistry and Materials Science, Hangzhou Institute for Advanced Study, University of Chinese Academy of Sciences, Hangzhou 310024, China

[5]These authors contributed equally

[6]Lead contact

*Correspondence: chendafujst@126.com (D.C.), xyliu@mail.sic.ac.cn (X.L.)

https://doi.org/10.1016/j.isci.2021.102226

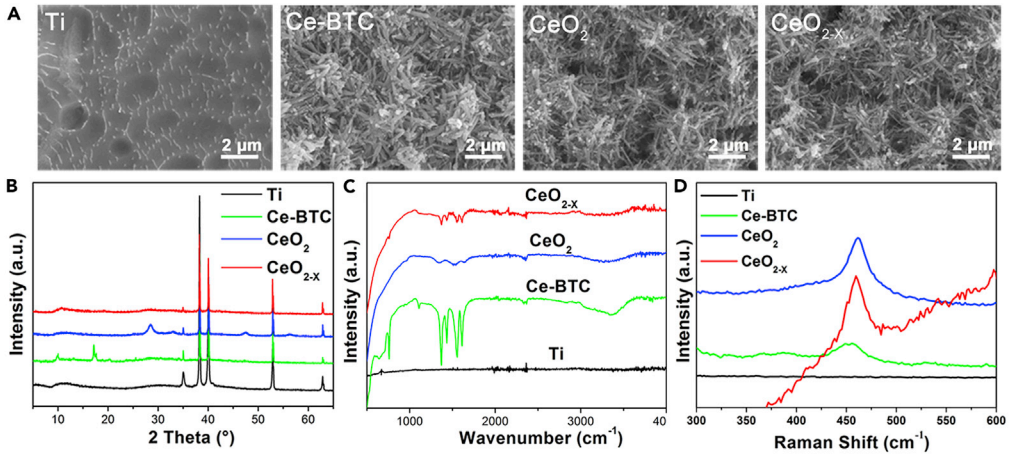

Figure 1. Material characterizations

(A) SEM surface morphology of Ti, Ce-BTC, CeO_2, and CeO_{2-X}. The scale bar is 2 μm.

(B) XRD patterns acquired from Ti, Ce-BTC, CeO_2, and CeO_{2-X}.

(C) FTIR spectra of Ti, Ce-BTC, CeO_2, and CeO_{2-X}.

(D) Raman spectra of Ti, Ce-BTC, CeO_2, and CeO_{2-X}.

oxide nanocrystals (Cao et al., 2018a; Rahul et al., 2015; Xiao et al., 2018). As for cerium oxide, the fraction of Ce (III) is size dependent and generally increases with decreases in the particle size. Therefore, in this work, cerium oxide films were fabricated on medical titanium surface by thermolysis of cerium-containing MOFs, and the Ce (III)/Ce (IV) ratio was regulated by conducting thermolysis process in the air or Ar atmosphere. Antibacterial activities of cerium oxide with different Ce (III)/Ce (IV) ratios were systematically investigated.

RESULTS

Surface characterization

Surface morphologies of Ti, Ce-BTC, CeO_2, and CeO_{2-X} are shown in Figure 1A. Ti presents a relatively flat surface with slight ups and downs after mixed acid cleaning. Ce-BTC exhibits rod-like morphology. After thermolysis in air, CeO_2 inherits the rod-like morphology with slight deformation. Similarly, CeO_{2-X} also shows a rod-like shape after pyrolysis in Ar atmosphere.

Figure 1B shows the X-ray diffraction (XRD) patterns of Ti, Ce-BTC, CeO_2, and CeO_{2-X}. Peaks located at 35.1°, 38.4°, 40.2°, and 53.0° correspond to the (100), (002), (101), and (102) facets of titanium, respectively (JCPDS Card No. 44-1,294). A peak of TiO_2 located at 62.8° appears which indicates that the TiO_2 oxide layer exists on the titanium substrate due to the natural oxidation. The diffraction patterns located at 10.1° and 17.2° suggest the high quality crystalline of the prepared Ce-BTC (Luo et al., 2018). CeO_2 sample shows a diffraction peak of (111) facet of ceria located at 28.5° indicating the thermolysis of organic ligands and change of valence states from Ce^{3+} to Ce^{4+} (He et al., 2020).

The Fourier transform infrared (FTIR) spectra of Ti, Ce-BTC, CeO_2, and CeO_{2-X} are presented in Figure 1C. No obvious peaks are observed from Ti. For Ce-BTC, characteristic peaks appear in the regions at 1,612 cm^{-1},550 cm^{-1} and 1,435 cm^{-1},369 cm^{-1} which correspond to the asymmetric vibrations (V_{as}(-COO-)) and symmetric vibrations (V_s(-COO-)), respectively (Zhang et al., 2018). After thermolysis in air, the feature peaks of Ce-BTC disappear in the CeO_2 sample. However, for the CeO_{2-X} sample with thermolysis in the Ar atmosphere, characteristic peaks in the regions 1,612 cm^{-1},550 cm^{-1} and 1,435 cm^{-1},369 cm^{-1} still remain, although the peak intensities decrease.

Figure 1D is the Raman spectra of Ti, Ce-BTC, CeO_2, and CeO_{2-X}. Ti sample exhibits a straight line with no peaks observed. For Ce-BTC, CeO_2, and CeO_{2-X} samples, a Raman peak at ~462 cm^{-1} is detected which is attributed to the F_{2g} vibration mode of O atoms around each Ce (IV) cation (Zhang et al., 2017).

The high-resolution X-ray photoelectron spectroscopy (XPS) spectra of Ce 3d acquired from Ce-BTC, CeO_2, and CeO_{2-X} are presented in Figures 2A–2C. The peaks located at 904.6 eV, 885.6 eV, and 880.8

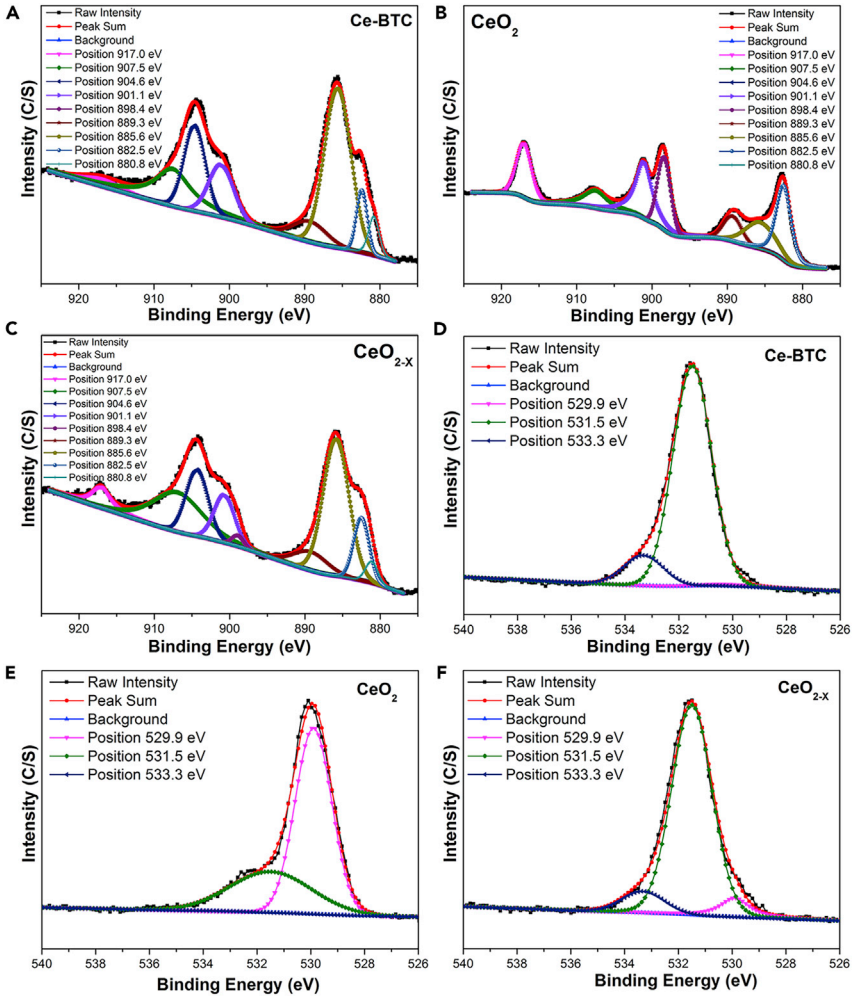

Figure 2. XPS high-resolution spectra of Ce 3d and O 1s

(A) XPS high-resolution spectrum of Ce 3d from Ce-BTC.

(B) XPS high-resolution spectrum of Ce 3d from CeO_2.

(C) XPS high-resolution spectrum of Ce 3d from CeO_{2-X}.

(D) XPS high-resolution spectrum of O 1s from Ce-BTC.

(E) XPS high-resolution spectrum of O 1s from CeO_2.

(F) XPS high-resolution spectrum of O 1s from CeO_{2-X}.

eV are assigned to Ce (III) and the peaks at 917.0 eV, 907.5 eV, 901.1 eV, 898.4 eV, 889.3 eV, and 882.5 eV belong to Ce (IV) (Tavarez-Martínez et al., 2019). By computing the areas of high-resolution XPS spectra of Ce 3d, the percentage content of Ce (III) can be obtained with the values of 57.0%, 12.7%, and 52.1% for Ce-BTC, CeO_2, and CeO_{2-X}, respectively (Table 1). It indicates that a higher Ce (III)/Ce (IV) ratio can be acquired after thermolysis in Ar atmosphere. Figures 2D–2F shows the high-resolution XPS spectra of O 1s from the surfaces of Ce-BTC, CeO_2, and CeO_{2-X}. The O 1s peaks can be divided into three sub-peaks at the binding energies of 529.9 eV, 531.4 eV, and 532.4 eV, which correspond to lattice oxygen (O_{Latt}), surface active oxygen (O_{Sur}), and adsorbed oxygen (O_{Ads}), respectively (He et al., 2020). The percent contents of O_{Latt}, O_{Sur}, and O_{Ads} were calculated by integrating the XPS peaks areas, and the results are shown in Table 1. The contents of O_{Latt} from Ce-BTC, CeO_2, and CeO_{2-X} are 0.6%, 74.1%, and 7.8%, respectively. O_{Sur} contents from Ce-BTC, CeO_2, and CeO_{2-X} are 58.4%, 15.5%, and 57.5%, respectively. For O_{Ads} contents, they are 41.0%, 10.4%, and 34.7% for Ce-BTC, CeO_2, and CeO_{2-X}, respectively. In general, oxygen vacancy is the indicator of the degree of lattice defects and it can be generated when high valent Ce ions can be converted into lower valent Ce ions. Accordingly, the increase of O_{Sur} contents can be ascribed to the formation of oxygen vacancies.

Table 1. Percentage contents of Ce (III) and Ce (IV) from Ce-BTC, CeO_2, and CeO_{2-X} and of O_{Latt}, O_{Sur}, and O_{Ads} from Ce-BTC, CeO_2, and CeO_{2-X}

	Ce valence concentration (%)		O 1s concentration (%)		
Samples	Ce (III)	Ce (IV)	O_{Latt}	O_{Sur}	O_{Ads}
Ce-BTC	57.0	43.0	0.6	58.4	41.0
CeO_2	12.7	87.3	74.1	15.5	10.4
CeO_{2-x}	52.1	47.9	7.8	57.5	34.7

Oxidase-like activity at different pH values

Many research studies have confirmed that ceria showed enzyme-mimicking activities, which are attributed to the valence states of Ce^{3+} and Ce^{4+}, as well as oxygen vacancies (Artiglia et al., 2014; Tian et al., 2015; Wei and Wang, 2013). To investigate the oxidase-like activity of Ce-BTC, CeO_2, and CeO_{2-X} at different pH values, TMB (3,3′,5,5′-tetramethylbenzidine) was used. TMB is a typical oxidase chromogenic substrate that can be oxidized to its colored product (oxidized TMB, TMB_{ox}) which has characteristic absorption peaks at 370 and 652 nm (Huang et al., 2017). Adsorption spectra from Ti, Ce-BTC, CeO_2, and CeO_{2-X} (pH = 6.0) are shown in Figure 3A. No peaks are observed from Ti, while characteristic peaks of TMB_{ox} at 370 and 652 nm are detected from Ce-BTC, which indicates that Ce-BTC has oxidase-like activity in acidic conditions. After pyrolysis in air, characteristic peaks of TMB_{ox} at 370 and 652 nm can still be obtained from CeO_2 while the adsorption intensities decrease. It suggests that the oxidase-like activity of CeO_2 is lower than that of Ce-BTC. However, adsorption intensities of TMB_{ox} at 370 and 652 nm from CeO_{2-X} significantly increase indicating the enhanced oxidase-like activity. The highest oxidase-like activity of CeO_{2-X} had also been confirmed in acetate buffer, PBS, and bacterial culture media (Figure S1). As presented in Figure 3B, when the reaction was carried out in an alkaline environment, the absorption spectra from Ce-BTC, CeO_2, and CeO_{2-X} do not show any obvious peaks at 370 and 652 nm. It indicates that TMB_{ox} is not produced, which confirms that catalytic reaction does not occur because of low oxidase-like activity in alkaline conditions.

ATP hydrolysis assay

Compounds based on lanthanide series including Ce-containing materials own high ATP deprivation ability which can hydrolyze ATP to release phosphate and adenosine leading to serious cell death. The ATP deprivation abilities of Ti, Ce-BTC, CeO_2, and CeO_{2-X} were investigated, and the corresponding results are shown in Figure 3C. The ATP deprivation contents of Ti, Ce-BTC, CeO_2, and CeO_{2-X} are 7.5%, 88.2%, 59.5%, and 97.7%, respectively. CeO_{2-X} has the highest ATP deprivation ability, followed by Ce-BTC and CeO_2. It indicates that, compared with Ce-BTC, the ATP deprivation ability of CeO_2 decreases while it increases for CeO_{2-X}. Moreover, the high ATP deprivation capacity of CeO_{2-X} was also verified in the bacterial growth medium and PBS (Figure S2).

ROS levels

To examine the ROS levels produced by Ti, Ce-BTC, CeO_2, and CeO_{2-X}, 2′,7′-dichlorodihydrofluorescein (DCFH) assay was used, and the results are presented in Figure 3D. At pH = 6.0, the ROS level of Ce-BTC is about 19 times than that of the black group. Compared with Ce-BTC, the ROS level of CeO_2 decreases which is about 6 times than that of the black group. However, CeO_{2-X} shows the highest ROS level which is approximately 62 times than that of the black group. At pH = 7.4, the abilities of ROS production of Ce-BTC, CeO_2, and CeO_{2-X} significantly decrease. It indicates that, in alkaline conditions, the catalytic activities of Ce-BTC, CeO_2, and CeO_{2-X} decline, especially for CeO_{2-X}.

Antibacterial activity assessment

Gram-negative *E. coli* and gram-positive *S. aureus* were applied to assess the antibacterial activities of Ti, Ce-BTC, CeO_2, and CeO_{2-X}. Plate colony counting and scanning electronic microscopy (SEM) cell morphology observation were carried out, and the results are presented in Figure 4. From Figure 4A, a lot of bacteria colonies of *S. aureus* can be seen from Ti. Compared with Ti, numbers of bacteria colonies from Ce-BTC, CeO_2, and CeO_{2-X} reduce, especially for CeO_{2-X} where almost no colonies are observed. Based on the plate colony counting results, antibacterial rates are obtained and presented

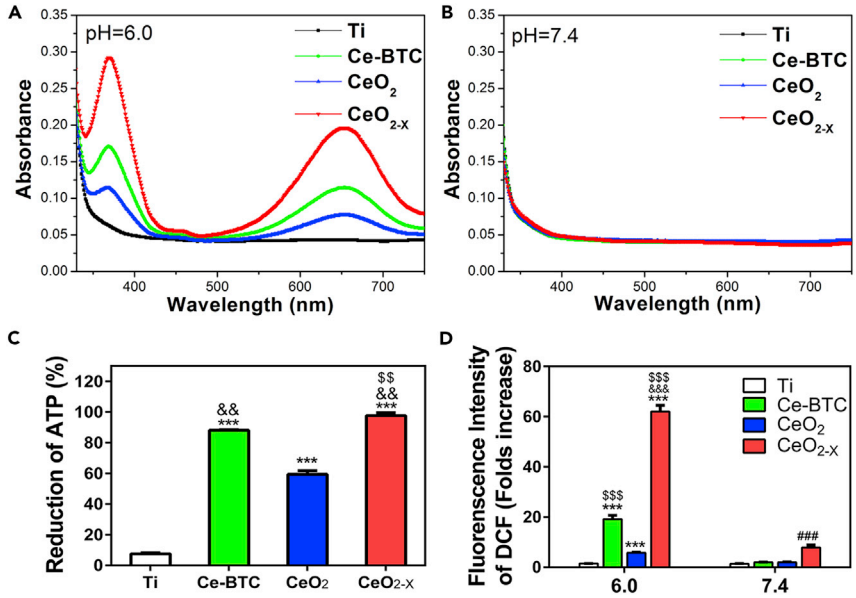

Figure 3. Oxidase-like activity, ATP hydrolysis ability, and ROS level assessment

(A) Catalytic activity of Ti, Ce-BTC, CeO_2, and CeO_{2-X} toward TMB at pH of 6.0.

(B) Catalytic activity of Ti, Ce-BTC, CeO_2, and CeO_{2-X} toward TMB at pH of 7.4.

(C) ATP hydrolysis ability of Ti, Ce-BTC, CeO_2, and CeO_{2-X}. ***$p < 0.001$ versus Ti; $^{\&\&}p < 0.01$ versus CeO_2; $^{\$\$}p < 0.01$ versus Ce-BTC.

(D) ROS levels produced from Ti, Ce-BTC, CeO_2, and CeO_{2-X}. ***$p < 0.001$ versus Ti; $^{\&\&\&}p < 0.001$ versus Ce-BTC; $^{\$\$\$}p < 0.001$ versus CeO_2; $^{\#\#\#}p < 0.001$ versus Ti.

See also Figures S1 and S2.

in Figure 4B. Antibacterial rates of Ce-BTC, CeO_2, and CeO_{2-X} are 46.2%, 9.7%, and 100%, respectively. It suggests that CeO_{2-X} exhibits the highest antibacterial rate, followed by Ce-BTC and CeO_2. Figure 4C shows the SEM morphologies of *S. aureus* from Ti, Ce-BTC, CeO_2, and CeO_{2-X}. *S. aureus* with round and intact morphology is observed from Ti. No significant change of cell morphology of *S. aureus* can be seen from Ce-BTC and CeO_2. However, *S. aureus* on CeO_{2-X} is dead with deformed and wizened cell morphology as indicated in red arrows. A similar trend can be obtained from *E. coli* on Ti, Ce-BTC, CeO_2, and CeO_{2-X}. Lots of bacteria colonies of *E. coli* can be seen from Ti, whereas bacteria numbers on Ce-BTC, CeO_2, and CeO_{2-X} decrease (Figure 4D). As shown in Figure 4E, the antibacterial rates of Ce-BTC, CeO_2, and CeO_{2-X} are 60.8%, 23.8%, and 91.6%, respectively. It indicates that CeO_{2-X} exhibits the highest antibacterial activity. SEM cell morphologies of *E. coli* from Ti, Ce-BTC, CeO_2, and CeO_{2-X} are presented in Figure 4F. Bacterial flagella of *E. coli* can be clearly seen from Ti which suggests that *E. coli* grow well on Ti. However, some bacteria with slight deformation can be observed from Ce-BTC and CeO_2 as shown in red arrows. For *E. coli* on CeO_{2-X}, they are badly wizened as presented in red arrows.

Cytocompatibility evaluation

MC3T3-E1 cells were used to evaluate the biocompatibility of Ti, Ce-BTC, CeO_2, and CeO_{2-X}. Figure 5A shows the cell live/dead staining fluorescence images of Ti, Ce-BTC, CeO_2, and CeO_{2-X}. Green fluorescence represents the live cells while red fluorescence indicates the dead cells. Lots of green fluorescence can be observed from Ti, Ce-BTC, CeO_2, and CeO_{2-X} while almost no red fluorescence can be seen, which indicates that Ti, Ce-BTC, CeO_2, and CeO_{2-X} have no cytotoxicity. AlamarBlue assay was used to assess the cell proliferation of Ti, Ce-BTC, CeO_2, and CeO_{2-X}, and the results are presented in Figure 5B. On day 1, there is no significant difference of cell proliferation among Ti, Ce-BTC, CeO_2, and CeO_{2-X}. With the extension of culture time, cell viabilities of Ti, Ce-BTC, CeO_2, and CeO_{2-X} increase. On day 7, Ce-BTC, CeO_2, and CeO_{2-X} present a higher cell proliferation rate than that of Ti ($p < 0.01$). Figure 5C shows the SEM cell morphologies of Ti, Ce-BTC, CeO_2, and CeO_{2-X} after culturing for 1, 4, and 7 days. Cells with the whole contour can be observed on Ti, Ce-BTC, CeO_2, and CeO_{2-X} after culturing for 1 day. As the culture time increases,

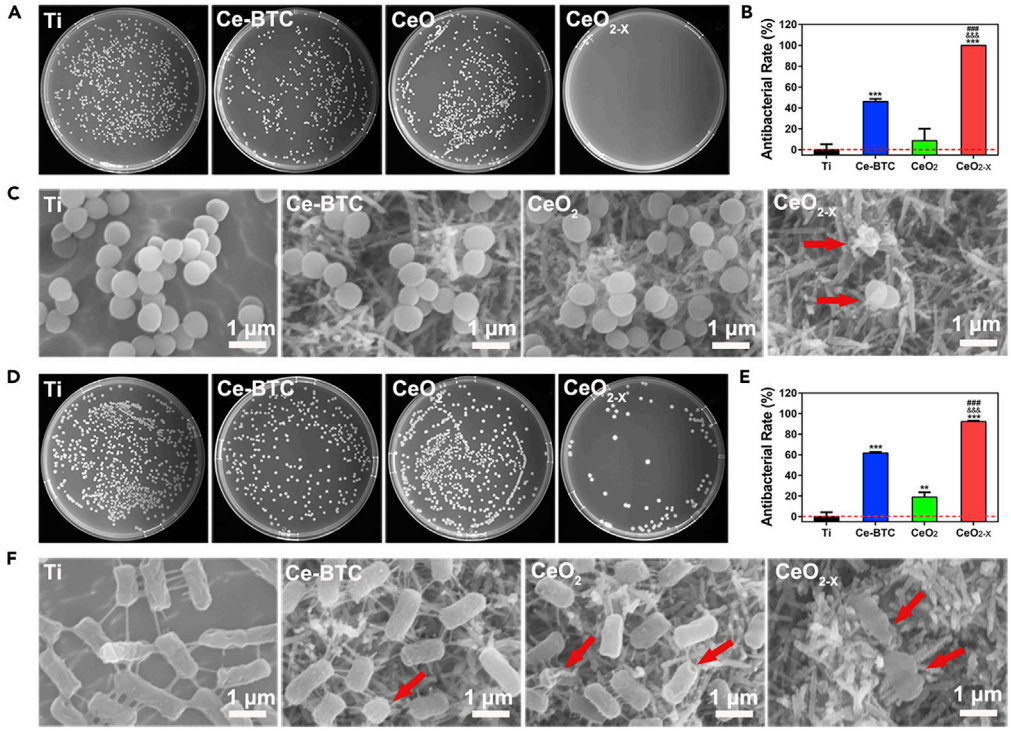

Figure 4. Antibacterial activity assessment

(A) Photographs of agar culture plates cultured with *S. aureus* suspension detached from Ti, Ce-BTC, CeO_2, and CeO_{2-X}.

(B) Antibacterial rates of Ti, Ce-BTC, CeO_2, and CeO_{2-X} against *S. aureus* based on the plate colony counting method. ***$p < 0.001$ versus Ti; $^{\&\&\&}p < 0.001$ versus CeO_2; $^{\$\$\$}p < 0.001$ versus Ce-BTC.

(C) SEM cell morphology of *S. aureus* on Ti, Ce-BTC, CeO_2, and CeO_{2-X}. The scale bar is 1 μm.

(D) Photographs of agar culture plates cultured with *E. coli* suspension detached from Ti, Ce-BTC, CeO_2, and CeO_{2-X}.

(E) Antibacterial rates of Ti, Ce-BTC, CeO_2, and CeO_{2-X} against *E. coli* based on the plate colony counting method. **$p < 0.01$ and ***$p < 0.001$ versus Ti; $^{\&\&\&}p < 0.001$ versus CeO_2; $^{\$\$\$}p < 0.001$ versus Ce-BTC.

(F) SEM cell morphology of *E. coli* on Ti, Ce-BTC, CeO_2, and CeO_{2-X}. The scale bar is 1 μm.

See also Figures S3 and S4.

cells grow and gradually cover the sample surface. On day 7, the cells almost cover the whole surfaces of Ti, Ce-BTC, CeO_2, and CeO_{2-X}. Based on the results of cell live/dead staining, cell proliferation, and cell morphology observation, it can be concluded that Ce-BTC, CeO_2, and CeO_{2-X} show good biocompatibility against MC3T3-E1 cells.

DISCUSSION

Ce-containing MOF pyrolysis strategy was used to obtain cerium oxide in the present study. The Raman peak at ~462 cm^{-1} was detected in Ce-BTC, CeO_2, and CeO_{2-X}, which indicated the existence of cerium oxygen clusters or cerium oxide nanocrystalline in those samples (Figure 1D). The characteristic peaks appear in the regions at 1,612 cm^{-1},550 cm^{-1} and 1,435 cm^{-1},369 cm^{-1} which corresponded to the vibrational modes of -COO- presented in the FTIR spectra of Ce-BTC nearly total vanished after thermolysis in air (Figure 1C). However, the characteristic peaks still remained although the peak intensities decreased after thermolysis in the Ar atmosphere, which indicated that the organic frameworks still existed after the incomplete carbonization of Ce-BTC. The XRD results showed that Ce-BTC could be converted into CeO_2 with high crystallinity after thermolysis in air, which may be originated from the aggregation of cerium oxide nanocrystals without the restriction of carbonaceous frameworks. On the contrary, due to the existence of carbonaceous frameworks and potential loose structure, cerium oxide nanocrystals were restricted to aggregate and exhibited relative weakly crystallized form (Cao et al., 2018a).

What's more, the proportion of Ce (III) in ceria nanoparticles is size dependent and generally increases with decreases in the particle size. Hence, modulation of valence states of cerium could be realized by thermolysis

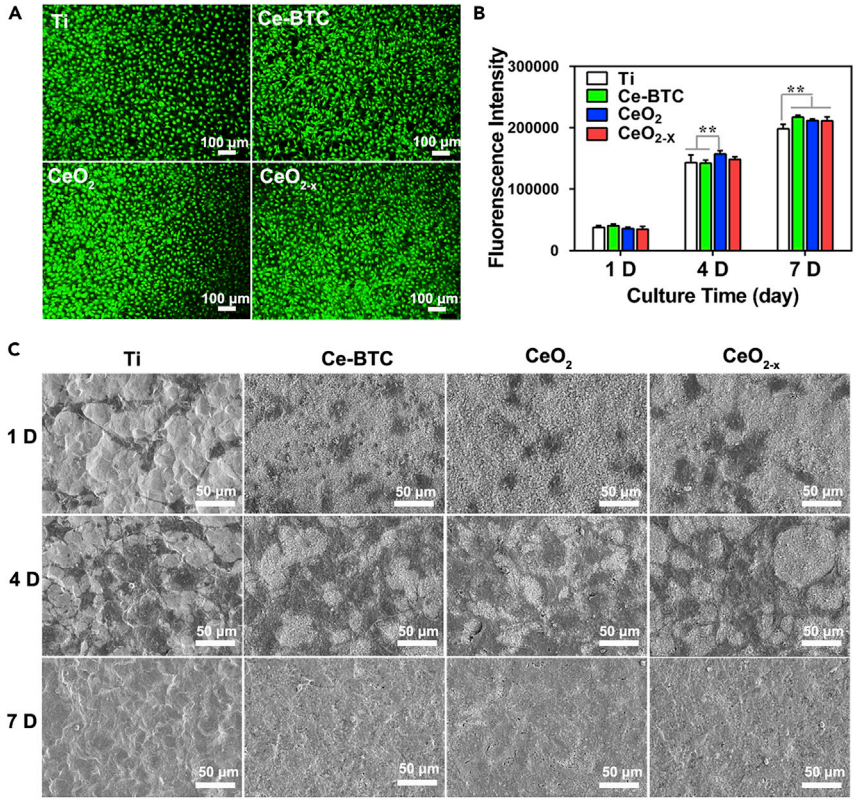

Figure 5. Biocompatibility evaluation

(A) Live/dead cell staining of MC3TC-E1 cells on Ti, Ce-BTC, CeO_2, and CeO_{2-X}. Green fluorescence represents live cells while red fluorescence indicates dead cells. The scale bar is 100 μm.

(B) Cell proliferation of MC3TC-E1 cells on Ti, Ce-BTC, CeO_2, and CeO_{2-X} after culturing for 1, 4, and 7 days. **$p < 0.01$.

(C) SEM cell morphologies of MC3TC-E1 cells on Ti, Ce-BTC, CeO_2, and CeO_{2-X} after culturing for 1, 4, and 7 days. The scale bar is 50 μm.

of Ce-containing MOFs in different gas environment by controlling the aggregation of cerium oxide nanocrystals. As shown in Figures 2 A–2C and Table 1, CeO_{2-X}, obtained by pyrolysis of Ce-BTC in Ar atmosphere, has the percentage content of Ce (III) with 52.1% whereas the percentage content of Ce (III) from CeO_2 with thermolysis of Ce-BTC in air is 12.7%. It indicates that Ce (III)/Ce (IV) ratio from CeO_{2-X} is much higher than that from CeO_2. Cerium oxide with a high Ce (III)/Ce (IV) ratio usually has abundant oxygen vacancies (Cao et al., 2018a; Vernekar et al., 2016). As presented in Figures 2D–2F and Table 1, O 1s high-resolution XPS spectra can be divided into three sub-peaks which correspond to lattice oxygen, surface active oxygen, and adsorbed oxygen. Low content of lattice oxygen and high content of surface active oxygen indicates a high concentration of oxygen vacancies. Thus, CeO_{2-X} has higher oxygen vacancy concentration than that of CeO_2 which can adsorb more O_2. Therefore, CeO_{2-X} has high percentage content of adsorbed oxygen with 34.7%.

The catalytic activity of cerium oxide is closely related to the content of Ce (III) and oxygen vacancies. At acidic pH of 6.0, Ce-BTC, CeO_2, and CeO_{2-X} can oxidize TMB to TMB_{OX} which show absorption peaks at 370 nm and 652 nm. It suggests the oxidase-like activity of Ce-BTC, CeO_2, and CeO_{2-X}. Due to the higher content of Ce (III) and oxygen vacancies, CeO_{2-X} exhibits higher adsorption intensity at 370 nm and 652 nm. Cheng et al.(Cheng et al., 2016) have investigated the reaction mechanism of oxidase-like activity. From their perspective, under acidic condition, O_2, adsorbed onto the cerium oxide surface, would be converted to $O_2^{\cdot-}$ by Ce (III) and TMB would be oxidized to TMB_{OX} by $O_2^{\cdot-}$. Meanwhile, Ce (IV) would be reduced to Ce (III) with the oxidation of TMB to TMB_{OX} and the reduced Ce (III) could be re-oxidized to Ce (IV) by $O_2^{\cdot-}$ *in situ*. However, at basic physiological pH of 7.4, oxidation of TMB did not occur (Figure 3B) and MC3TC-E1

cells grew well on Ce-BTC, CeO_2, and CeO_{2-X} (Figure 5). Based on this, it can be concluded that, at acidic pH, Ce (III)/Ce (IV) couple serves as prooxidant for the production of ROS and the effect would be enhanced with the increase of Ce (III)/Ce (IV) ratio. ROS levels produced by Ti, Ce-BTC, CeO_2, and CeO_{2-X} further confirm this view (Figure 3D). Besides, compounds based on lanthanide series including Ce-containing materials own high ATP deprivation ability by hydrolyzing ATP to release phosphate and adenosine which can cut off the energy supply and lead to serious cell death. As shown in Figure 3C, CeO_{2-X} shows the highest ATP deprivation ability, followed by Ce-BTC and CeO_2.

The antibacterial mechanisms of CeO_2 nanoparticles proposed in most literatures are the electrostatic attraction between CeO_2 nanoparticles and bacteria where CeO_2 nanoparticles are positively charged and bacteria are negatively charged, leading to oxidative stress and interfering with the nutrient transport functions (Nadeem et al., 2020; Qi et al., 2020; Zhang et al., 2019). Moreover, the antibacterial effects of CeO_2 nanoparticles against *S. aureus* and *E. coli* are different, which is closely related to cell membrane structures. In general, gram-positive bacteria are composed of thicker, waxy cell wall, making them more resistant to the CeO_2 nanoparticles than gram-negative bacteria. For example, the gram-positive *Bacillus cereus* has a cell wall of 55.4 nm, while the gram-negative *S. typhimurium* has a cell wall of only 2.4 nm (Kalantari et al., 2020; Pop et al., 2020). However, in this study, bacteria are living well on CeO_2, meaning that the electrostatic attraction between CeO_2 and bacteria is not the main antibacterial factor. Besides, antibacterial rate of CeO_{2-X} against *S. aureus* is higher than that to *E. coli*, which further confirms that the antibacterial mechanism mentioned above is not suitable here. Results of agar diffusion assay (Figure S3) showed that no inhibition zone could be seen around the samples which suggested that CeO_2 species leached into the growth medium during the bacterial growth were negligible to the antibacterial effects. The pH of bacterial culture media (Luria-Bertani medium and Nutrient Broth No.2 medium) used in this study was weakly acidic (Figure S4), and the oxidase-like activity of Ce-BTC, CeO_2, and CeO_{2-X} had been confirmed in acetate buffer, PBS, and bacterial culture media with the similar pH (Figure S1). Moreover, the high ATP deprivation capacity of CeO_{2-X} was also verified in the bacterial growth medium and PBS, and the ATP deprivation capacity of CeO_{2-X} had no significant difference at pH of 6.0 and 7.4 which were similar to the pH of bacterial culture medium and cell culture medium in this study, respectively (Figure S2). Compared with Ce-BTC and CeO_2, the oxidase-like activity and ATP deprivation ability of CeO_{2-X} were the highest, which corresponded to the highest antibacterial rate against *S. aureus* and *E. coli*. Therefore, we believe that CeO_{2-X} shows antibacterial activity which is ascribed to the both oxidase-like activity by producing ROS in the acidic bacterial environment and ATP deprivation ability. Based on the results in this study, it can be seen that the antibacterial activity of cerium oxide can be tailed by regulating of Ce (III)/Ce (IV) ratio which higher Ce (III)/Ce (IV) ratio indicates higher ROS levels and ATP deprivation capacity leading to higher antibacterial activity. Although the percentage content of Ce (III) from Ce-BTC is slightly higher than that from CeO_{2-X}, the central Ce atom on Ce-BTC is nine coordinated by six oxygen atoms from water molecule and three oxygen atoms from the carboxylate groups of 1,3,5-H_3BTC ligands, leading to less active sites (Zhang et al., 2018). Therefore, the oxidase-like activity and ATP deprivation capacity of Ce-BTC are lower than those of CeO_{2-X}.

The biocompatibility of Ce-BTC, CeO_2, and CeO_{2-X} was also investigated in this study. Interestingly, the oxidase-like activity of Ce-BTC, CeO_2 and CeO_{2-X} is pH dependent, and the oxidation of TMB by Ce-BTC, CeO_2, and CeO_{2-X} can only occur under acidic conditions. Thus, in the weak alkaline environment of cell culture medium, the generation of ROS can be negligible. Moreover, the CeO_2-based coating can directly contact the bacterial membrane and cut off the energy supply of bacteria. However, mammalian-based cells are much bigger than bacteria cells, and the mitochondria serve as the main organelles in the production of ATP for the mammalian-based cells which is membrane bounded into a more complex endomembrane system (Cao et al., 2011). It is difficult for CeO_2-based coating to interfere with the ATP synthesized in mammalian-based cells. Therefore, Ce-BTC, CeO_2, and CeO_{2-X} showed negligible side effects to MC3T3-E1 cells.

In conclusion, cerium oxide was fabricated on the medical titanium surface by pyrolysis of Ce-BTC, and regulation of Ce (III)/Ce (IV) ratio was realized by thermolysis of Ce-BTC in different gas environment. CeO_{2-X}, obtained by thermolysis of Ce-BTC in Ar atmosphere, has higher Ce (III) content and oxygen vacancies than those of CeO_2 with thermolysis of Ce-BTC in air. Therefore, CeO_{2-X} shows a higher ROS level and ATP deprivation capacity which exhibits superior antibacterial activity.

Limitations of the study

In this study, cerium oxide with alterable ratios of Ce (III)/Ce (IV) was constructed on titanium surface by pyrolysis of Ce-BTC in different gas atmosphere. However, the cerium-oxygen clusters in Ce-BTC will inevitably agglomerate together to form ceria nanoparticles during the pyrolysis process. The enzyme-like catalytic activity of cerium oxide will be partially inhibited when the content of surface oxygen vacancies decreases as the nanoparticles grow up. Moreover, only *S. aureus* and *E. coli* were used to evaluate the antibacterial properties in this study, and broad-spectrum antibacterial effect should be further investigated.

Resource availability

Lead contact

Dafu Chen: chendafujst@126.com Xuanyong Liu: xyliu@mail.sic.ac.cn.

Material availability

This study did not generate new unique reagents.

Data and code availability

This study did not generate data sets/code.

METHODS

All methods can be found in the accompanying Transparent methods supplemental file.

SUPPLEMENTAL INFORMATION

Supplemental information can be found online at https://doi.org/10.1016/j.isci.2021.102226.

ACKNOWLEDGMENTS

This study acknowledged financial support from the National Natural Science Foundation of China (51831011, 31670980), National Science Fund for Distinguished Young Scholars of China (51525207), Science and Technology Commission of Shanghai Municipality (19JC1415500, 20ZR1465100), and Beijing Municipal Health Commission (Grant No. BMHC-2019-9 ; BMHC-2018-4 ; PXM2020_026275_000002).

AUTHOR CONTRIBUTIONS

X.L., J.Q., and H.Z. participated in the conception and design of the research. H.Z., B.Y., and L.L. performed the experiments. J.Q. and H.Z. prepared the manuscript. D.C. and X.L. revised the manuscript.

DECLARATION OF INTERESTS

The authors declare no competing financial interests.

Received: September 30, 2020
Revised: December 21, 2020
Accepted: February 19, 2021
Published: March 19, 2021

REFERENCES

Artiglia, L., Agnoli, S., Paganini, M.C., Cattelan, M., and Granozzi, G. (2014). TiO_2@CeOx core-shell nanoparticles as artificial enzymes with peroxidase-like activity. ACS Appl. Mater. Interfaces *6*, 20130–20136.

Cao, H., Liu, X., Meng, F., and Chu, P.K. (2011). Biological actions of silver nanoparticles embedded in titanium controlled by micro-galvanic effects. Biomaterials *32*, 693–705.

Cao, F., Zhang, Y., Sun, Y., Wang, Z., Zhang, L., Huang, Y., Liu, C., Liu, Z., Ren, J., and Qu, X. (2018a). Ultrasmall nanozymes isolated within porous carbonaceous frameworks for synergistic cancer therapy: enhanced oxidative damage and reduced energy supply. Chem. Mater. *30*, 7831–7839.

Cao, H.L., Tang, K.W., and Liu, X.Y. (2018b). Bifunctional galvanics mediated selective toxicity on titanium. Mater. Horiz. *5*, 264–267.

Chen, Z., Wang, Z., Ren, J., and Qu, X. (2018). Enzyme mimicry for combating bacteria and biofilms. Acc. Chem. Res. *51*, 789–799.

Cheng, H., Lin, S., Muhammad, F., Lin, Y.-W., and Wei, H. (2016). Rationally modulate the oxidase-like activity of nanoceria for self-regulated bioassays. ACS Sensors *1*, 1336–1343.

Dong, W., and Huang, Y. (2019). CeO_2/C nanowire derived from a cerium(III) based organic framework as a peroxidase mimic for colorimetric sensing of hydrogen peroxide and for enzymatic sensing of glucose. Microchim. Acta *187*, 11.

Gupta, A., Sakthivel, T.S., Neal, C.J., Koul, S., Singh, S., Kushima, A., and Seal, S. (2019). Antioxidant properties of ALD grown nanoceria

films with tunable valency. Biomater. Sci. *7*, 3051–3061.

He, J., Xu, Y., Shao, P., Yang, L., Sun, Y., Yang, Y., Cui, F., and Wang, W. (2020). Modulation of coordinative unsaturation degree and valence state for cerium-based adsorbent to boost phosphate adsorption. Chem. Eng. J. *394*, 124912.

Hu, Z., Guo, Z., Zhang, Z., Dou, M., and Wang, F. (2018). Bimetal zeolitic imidazolite framework-derived iron-, cobalt- and nitrogen-codoped carbon nanopolyhedra electrocatalyst for efficient oxygen reduction. ACS Appl. Mater. Interfaces *10*, 12651–12658.

Huang, L., Zhang, W., Chen, K., Zhu, W., Liu, X., Wang, R., Zhang, X., Hu, N., Suo, Y., and Wang, J. (2017). Facet-selective response of trigger molecule to CeO_2 {1 1 0} for up-regulating oxidase-like activity. Chem. Eng. J. *330*, 746–752.

Kalantari, K., Mostafavi, E., Saleh, B., Soltantabar, P., and Webster, T.J. (2020). Chitosan/PVA hydrogels incorporated with green synthesized cerium oxide nanoparticles for wound healing applications. Eur. Polym. J. *134*, 109853.

Li, J.Y., Zhai, D., Lv, F., Yu, Q.Q., Ma, H.S., Yin, J.B., Yi, Z.F., Liu, M.Y., Chang, J., and Wu, C.T. (2016). Preparation of copper-containing bioactive glass/eggshell membrane nanocomposites for improving angiogenesis, antibacterial activity and wound healing. Acta Biomater. *36*, 254–266.

Li, S., Wang, N., Yue, Y., Wang, G., Zu, Z., and Zhang, Y. (2015). Copper doped ceria porous nanostructures towards a highly efficient bifunctional catalyst for carbon monoxide and nitric oxide elimination. Chem. Sci. *6*, 2495–2500.

Li, B., Ma, J.W., Wang, D.H., Liu, X.Y., Li, H.P., Zhou, L.X., Liang, C.Y., and Wang, H.S. (2019a). Self-adjusting antibacterial properties of Ag-incorporated nanotubes on micro-nanostructured Ti surfaces. Biomater. Sci. *7*, 4075–4087.

Li, X., Qi, M., Sun, X., Weir, M.D., Tay, F.R., Oates, T.W., Dong, B., Zhou, Y., Wang, L., and Xu, H.H.K. (2019b). Surface treatments on titanium implants via nanostructured ceria for antibacterial and anti-inflammatory capabilities. Acta Biomater. *94*, 627–643.

Luo, J., Cui, J., Wang, Y., Yu, D., Qin, Y., Zheng, H., Hong, Y., Zhang, Y., and Wu, Y. (2018). MOF-derived porous CeO_{2-x}/C nanorods and their applications in uric acid biosensor. Nano *13*, 1850085.

Mehmood, R., Ariotti, N., Yang, J.L., Koshy, P., and Sorrell, C.C. (2018). pH-responsive morphology-controlled redox behavior and cellular uptake of nanoceria in fibrosarcoma. ACS Biomater. Sci. Eng. *4*, 1064–1072.

Nadeem, M., Khan, R., Afridi, K., Nadhman, A., Ullah, S., Faisal, S., Mabood, Z.U., Hano, C., and Abbasi, B.H. (2020). Green synthesis of cerium oxide nanoparticles (CeO_2 NPs) and their antimicrobial applications: a review. Int. J. Nanomed. *15*, 5951–5961.

Pop, O.L., Mesaros, A., Vodnar, D.C., Suharoschi, R., Tăbăran, F., Mageruşan, L., Tódor, I.S., Diaconeasa, Z., Balint, A., and Ciontea, L. (2020). Cerium oxide nanoparticles and their efficient antibacterial application in vitro against gram-positive and gram-negative pathogens. Nanomaterials *10*, 1614.

Qi, M., Li, W., Zheng, X., Li, X., Sun, Y., Wang, Y., Li, C., and Wang, L. (2020). Cerium and its oxidant-based nanomaterials for antibacterial applications: a state-of-the-art review. Front. Mater. *7*, 213.

Rahul, R., Salunkhe, J.T., Kamachi, Y., Nakato, T., Kim, J.H., and Yamauchi, Y. (2015). Asymmetric supercapacitors using 3D nanoporous carbon and cobalt oxide electrodes synthesized from a single metal organic framework. ACS Nano *9*, 6288–6296.

Shao, D., Li, K., You, M., Liu, S., Hu, T., Huang, L., Xie, Y., and Zheng, X. (2020). Macrophage polarization by plasma sprayed ceria coatings on titanium-based implants: cerium valence state matters. Appl. Surf. Sci. *504*, 144070.

Sirelkhatim, A., Mahmud, S., Seeni, A., Kaus, N.H.M., Ann, L.C., Bakhori, S.K.M., Hasan, H., and Mohamad, D. (2015). Review on zinc oxide nanoparticles: antibacterial activity and toxicity mechanism. Nano Micro Lett. *7*, 219–242.

Tavarez-Martínez, G.M., Onofre-Bustamante, E., De La Cruz-Terrazas, E.C., Escudero-Rincón, M.L., and Domínguez-Crespo, M.A. (2019). Evaluation of TiO_2/CeO_2 coating on Ti6Al4V alloy in PBS physiological medium using conventional and near field electrochemical techniques. Appl. Surf. Sci. *494*, 1109–1118.

Tian, Z.M., Li, J., Zhang, Z.Y., Gao, W., Zhou, X.M., and Qu, Y.Q. (2015). Highly sensitive and robust peroxidase-like activity of porous nanorods of ceria and their application for breast cancer detection. Biomaterials *59*, 116–124.

Vernekar, A.A., Das, T., and Mugesh, G. (2016). Vacancy-engineered nanoceria: enzyme mimetic hotspots for the degradation of nerve agents. Angew. Chem. Int. Ed. *55*, 1412–1416.

Wei, H., and Wang, E.K. (2013). Nanomaterials with enzyme-like characteristics (nanozymes): next-generation artificial enzymes. Chem. Soc. Rev. *42*, 6060–6093.

Wright, G.D. (2011). Molecular mechanisms of antibiotic resistance. Chem. Commun. *47*, 4055.

Xia, C., Ma, X.H., Zhang, X.M., Li, K.Q., Tan, J., Qiao, Y.Q., and Liu, X.Y. (2020). Enhanced physicochemical and biological properties of C/Cu dual ions implanted medical titanium. Bioact. Mater. *5*, 377–386.

Xiao, L., Xu, R., and Wang, F. (2018). Facile synthesis of CoxP decorated porous carbon microspheres for ultrasensitive detection of 4-nitrophenol. Talanta *179*, 448–455.

Yang, T.T., Wang, D.H., and Liu, X.Y. (2020). Antibacterial activity of an NIR-induced Zn ion release film. J. Mater. Chem. B *8*, 406–415.

Zhang, M., Zhang, C., Zhai, X., Luo, F., Du, Y., and Yan, C. (2019). Antibacterial mechanism and activity of cerium oxide nanoparticles. Sci. China Mater. *62*, 1727–1739.

Zhang, X., Hou, F., Li, H., Yang, Y., Wang, Y., Liu, N., and Yang, Y. (2018). A strawsheave-like metal organic framework Ce-BTC derivative containing high specific surface area for improving the catalytic activity of CO oxidation reaction. Microporous Mesoporous Mater. *259*, 211–219.

Zhang, X., Hou, F., Yang, Y., Wang, Y., Liu, N., Chen, D., and Yang, Y. (2017). A facile synthesis for cauliflower like CeO_2 catalysts from Ce-BTC precursor and their catalytic performance for CO oxidation. Appl. Surf. Sci. *423*, 771–779.

iScience, Volume *24*

Supplemental information

Regulation of Ce (III) / Ce (IV) ratio of cerium oxide for antibacterial application

Haifeng Zhang, Jiajun Qiu, Bangcheng Yan, Lidan Liu, Dafu Chen, and Xuanyong Liu

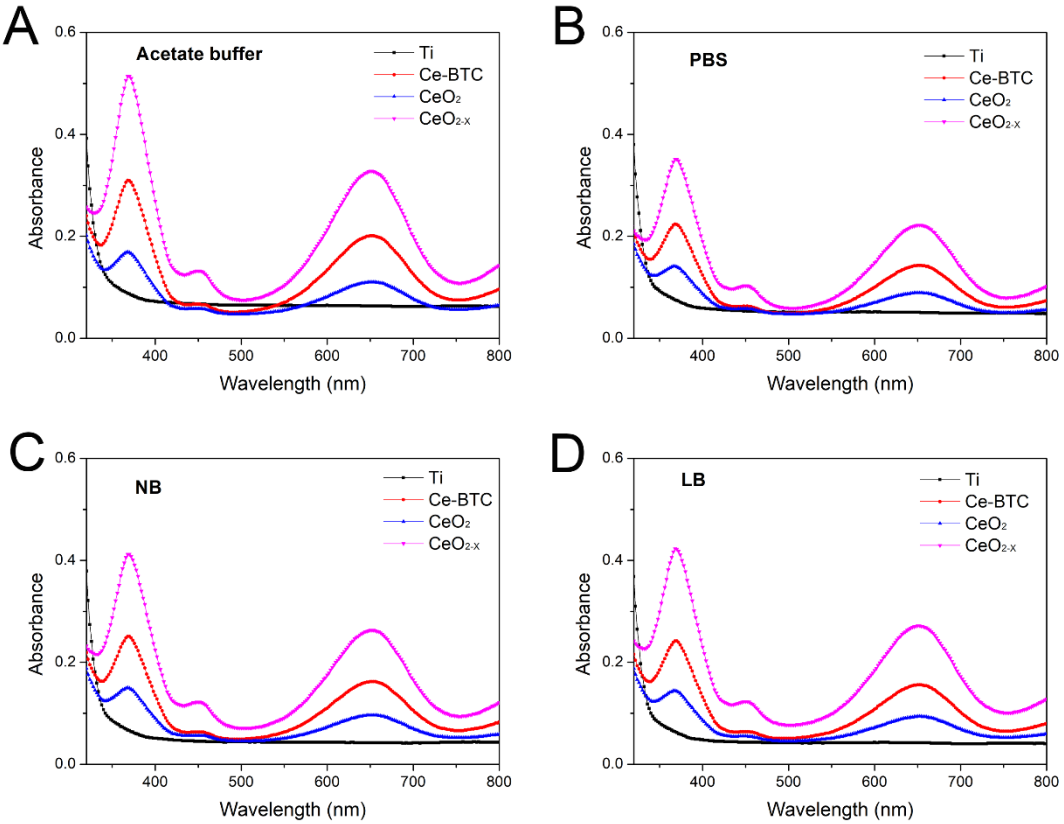

Figure S1. Catalytic activity of Ti, Ce-BTC, CeO_2 and CeO_{2-x} towards TMB in acetate buffer (A), PBS (B), Nutrient Broth No.2 medium (C), and Luria-Bertani medium (D). Related to Figure 3. The oxidase-like activities of various samples were investigated in different biological buffers similar to pH of the growth media (weakly acidic environment). The results showed that TMB could be oxidized to its colored product TMBox in different buffers, including acetate buffer, PBS, Luria-Bertani medium and Nutrient Broth No.2 medium.

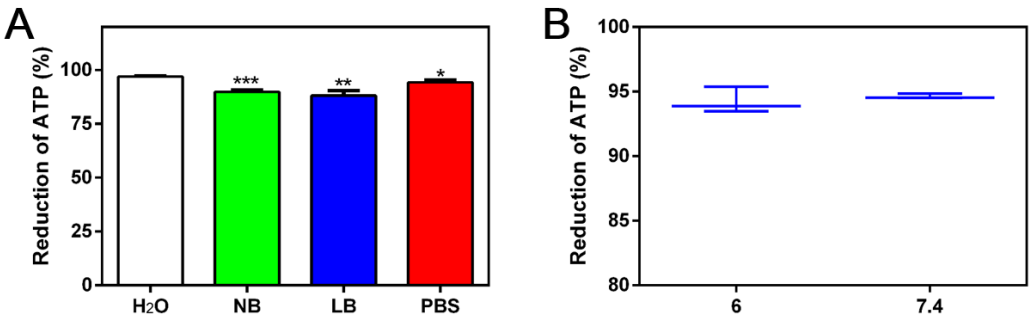

Figure S2. (A) ATP hydrolysis ability of CeO_{2-X} in aqueous solution, NB medium, LB medium, and PBS; (B) ATP hydrolysis ability of CeO_{2-X} in PBS with different pH. Related to Figure 3. The ATP deprivation assay was also conducted in bacterial growth medium (Nutrient Broth No.2 (NB) medium and Luria-Bertani (LB) medium) and PBS. As shown in Figure S4A, the ATP deprivation contents of CeO_{2-X} was 96.9% in aqueous solution, 89.8% in NB medium, 88.2% in LB medium, and 94.2% in PBS, respectively, which indicated that bacterial medium had slight influence on the ATP deprivation ability of CeO_{2-X}. The result in Figure S4B showed that ATP deprivation contents of CeO_{2-X} in PBS were 94.2% at pH=6 and 94.6% at pH=7.4, which implied the ATP deprivation ability of CeO_{2-X} had no significant difference at pH of 6.0 and 7.4 in this study.

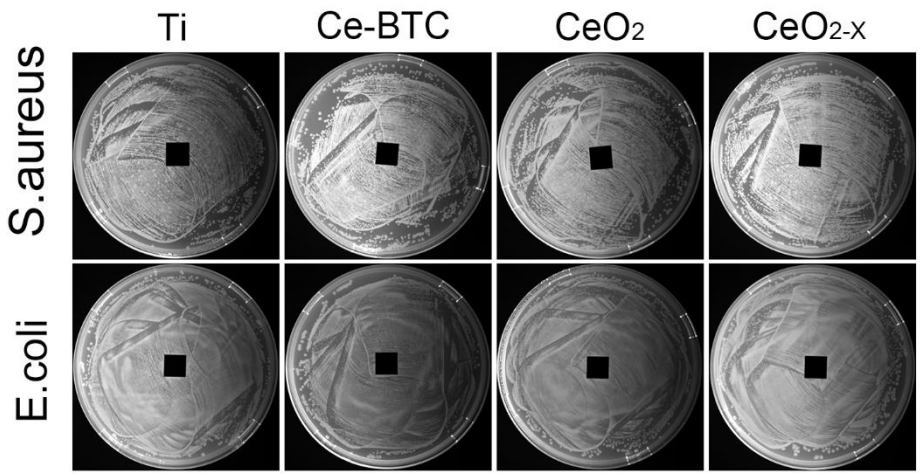

Figure S3. Inhibition zones around different samples against *S. aureus* and *E. coli*.

Related to Figure 4. The agar diffusion was performed as followed: bacterial suspension (100 μL, 10^7 cfu mL^{-1}) was introduced to the standard Nutrient Broth No.2 or Luria-Bertani agar culture medium where the samples were put subsequently, followed by incubation at 37 °C for 24 h. The result showed that no inhibition zone could be seen around the samples which suggested that CeO_2-species leached into the growth medium during the bacterial growth were negligible to the antibacterial effects.

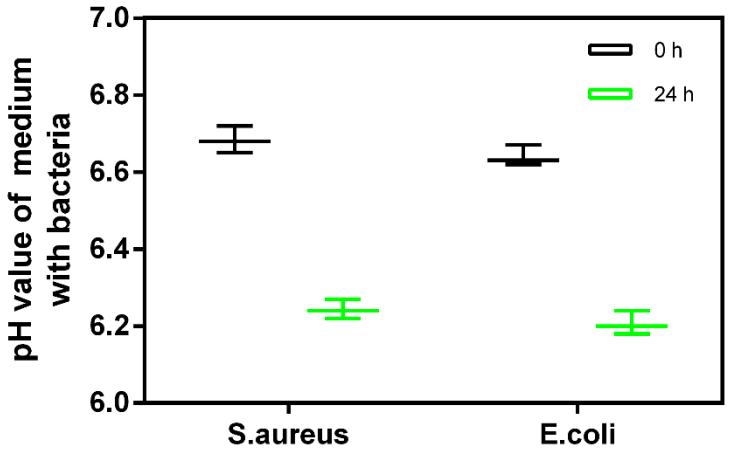

Figure S4. pH changes of bacterial medium with *S. aureus* or *E. coli*. Related to Figure 4. The pH of bacterial culture media used in this study were weakly acidic and further decreased as the culture time extended, which may be resulted from the bacteria metabolism products.

Transparent Methods

Materials

Commercial pure titanium plates (Cp Ti, Grade 2) with dimensions of 10 mm × 10 mm × 1 mm were purchased from Xi'an Saite Metal Materials Development Co. Ltd, China. Trimesic acid (H_3BTC, 98%), cerium nitrate hexahydrate ($Ce(NO_3)_3 \cdot 6H_2O$, 99.95% metals basis) and Hexamethyldisilazane (HMDS, 98%) were bought from Aladdin Industrial Co. (Shanghai, China). Potassium hydroxide (KOH, AR), ethanol absolute (≥99.7%), N, N-Dimethylformamide (DMF, ≥99.5%), and Hydrofluoric acid (HF, ≥40.0%) were purchased from Shanghai Lingfeng Chemical Reagents Co., Ltd, Shanghai, China. Nitric acid (HNO_3, AR) and Glacial acetic acid (AR) were obtained from HUSHI, Shanghai, China. 2',7'-Dichlorodihydrofluorescein diacetate was provided by Sigma Chemical Co. (MO, USA). Glutaraldehyde solution (25%) was purchased from Sinooharm Group Co. LTD., Beijing, China. 3,3',5,5'-Tetramethylbenzidine (TMB, 98%) was provided by damas-beta (Shanghai, China). ATP and ATP Assay Kit were obtained from Beyotime Biotechnology, Shanghai, China. All reagents were used as received without further purification. The water used in all experiments was purified by a Millipore system.

Experimental section

Preparation of Ce-BTC on titanium surface

Commercial pure titanium plates with dimensions of 10 mm × 10 mm × 1 mm were cleaned with mixed HF and HNO_3 aqueous solution to eliminate the surface

contaminants, followed by ultrasonically cleaning in ethanol and ultrapure water. The corresponding samples were denoted as Ti. Then, Ti samples were pre-treated with 5M KOH solutions at 80 ℃ for 6 h. Ce-BTC was fabricated on pre-treated titanium surface via solvothermal reaction and the detailed experimental operation is as follows. First, 31.5 mg of H_3BTC and 217 mg of $Ce(NO_3)_3 \cdot 6H_2O$ were dissolved in 50 mL of DMF. Next, pre-treated Ti samples were soaked in the mixture solution and sealed in a 100 mL Teflon-lined stainless-steel autoclave and reacted at 120 ℃ for 18 h. Finally, the samples were collected and cleaned with ultrapure water and ethanol under an ultrasonic condition, and the corresponding samples were denoted as Ce-BTC.

Preparation of CeO_2 and CeO_{2-X}

The as-obtained Ce-BTC samples were put into a muffle furnace and heated at 450 ℃ for 2 h in an ambient atmosphere with a heating rate of 5 ℃/min. At last, the samples were cooled down to room temperature and the corresponding samples are named as CeO_2. To obtain a high Ce^{3+}/Ce^{4+} ratio of cerium oxide with more oxygen vacancies, the as-obtained Ce-BTC samples were put into a tube furnace and heated at 450 ℃ for 2 h in Ar atmosphere (10 sccm) with the heating rate of 5 ℃/min. Finally, the samples were cooled down to room temperature and labeled as CeO_{2-X}.

Materials Characterization

Surface morphologies of Ti, Ce-BTC, CeO_2, and CeO_{2-x} were examined by Tungsten filament scanning electron microscopy (SEM; S-3400N, HITACHI, Japan). X-ray

diffraction (XRD, D2, Bruker, Germany) with Cu Kα radiation (λ = 0.154 nm) was applied to detect the phase structures of the samples. The chemical compositions and valence states of the sample surfaces were analyzed via X-ray photoelectron spectroscopy (XPS, RBD upgraded PHI-5000C ESCA system, Perkin Elmer, USA). Fourier transform infrared (FTIR) analyses were measured on a Bruker Tensor 27 FTIR spectrometer. Raman spectroscopy characterizations were carried out using a Raman microscope system (LabRAM, Horiba Jobin Yvon, France) with a 514.5 nm laser source.

Oxidase-Like Activity Assessment

The oxidase-like activities of Ti, Ce-BTC, CeO_2, and CeO_{2-x} were studied by evaluating the catalytic performance of TMB in acetate buffer. In brief, Ti, Ce-BTC, CeO_2, and CeO_{2-x} were placed in a 24-well plate and 980 μL of acetate buffer (0.2 M, pH values are 6.0 and 7.4, respectively) were added. Subsequently, 20 μL of TMB solution (40 mM) was added and incubated at room temperature for 30 min. At last, 100 μL of the solution mentioned above was pipetted and transformed to a 96-well black plate and the absorbance was measured by Cytation 5 Multi-Mode Reader (BioTek, USA).

Detection of Reactive Oxygen Species (ROS)

ROS levels generated by Ti, Ce-BTC, CeO_2, and CeO_{2-x} were detected by DCFH-DA assay. In detail, 0.5 mL of DCFH-DA (20 mM) was reacted with 2 mL of NaOH (0.01M) for 30 min at room temperature in the dark. Subsequently, the reaction was stopped by

adding 10 mL of acetate buffer (0.2 M, pH 7.0) and then DCFH was obtained. Afterwards, Ti, Ce-BTC, CeO_2, and CeO_{2-x} were immersed in 950 μL of acetate buffer with pH = 6.0 and 7.4, followed by adding 50 μL of DCFH solution. After incubation for 90 min at room temperature in the dark, 100 uL of the as-mentioned solution was pipetted and transformed to a 96-well black plate, and the fluorescence intensity was examined by Cytation 5 Multi-Mode Reader with an excitation wavelength of 488 nm and an emission wavelength of 525 nm. The final result was expressed as the folds increase of fluorescence intensity to the control sample (Ti).

ATP Deprivation Evaluation

To evaluate the ATP deprivation properties of Ti, Ce-BTC, CeO_2, and $CeO_{2-x,}$ an APT assay kit was used. First, Ti, Ce-BTC, CeO_2, and CeO_{2-x} were placed in a 24-well plate and incubated with 1 mL of ATP aqueous solution (200 μM) at 37 ℃ for 12 h in the dark. After that, the ATP contents remained were determined by the ATP assay kit. In detail, the luminescence of the solutions was detected by Cytation 5 Multi-Mode Reader and the ATP concentration remained in solutions were calculated according to a standard curve.

Antibacterial activity evaluation

Bacterial culture

Gram-positive *Staphylococcus aureus* (*S. aureus*, ATCC 25923) and Gram-negative *Escherichia coli* (*E. coli*, ATCC 25922) were applied to investigate the antibacterial

activity of various samples. Luria-Bertani medium and Nutrient Broth No.2 medium were used for bacterial culture of *E. coli* and *S. aureus*, respectively. Before the inoculation of bacteria on sample surfaces, all the samples were sterilized with 75 vol% alcohol for 2 h and dried on the super clean bench. Afterwards, 60 μL of bacterial suspensions (10^7 CFU mL^{-1}) was dropped onto Ti, Ce-BTC, CeO_2, and CeO_{2-x} and cultured for 24 h at 37 °C.

Plate Colony Counting

To quantitatively characterize the antibacterial ability of Ti, Ce-BTC, CeO_2, and CeO_{2-x}, plate colony counting experiments were performed. To be specific, when bacteria cultured on the sample surfaces for 24 h, the samples with bacterial suspension were transformed into test tubes with 4 mL of physiological saline, and shaken for 1 min to detach the bacteria from the sample surfaces. Then, the obtained bacterial suspension was diluted with physiological saline. Subsequently, 100 μL of the diluted bacterial suspension was introduced to a standard agar culture plate and cultured for another 18 h at 37℃. At last, photos of agar culture plates were taken and colonies were counted. The antibacterial ratio was calculated as the following equation

$$\text{Antibacterial ratio } (\%) = \frac{A - B}{A} \times 100\%$$

Where A and B denote the average number of colonies (CFU per sample) on the control group (Ti) and test groups (Ce-BTC, CeO_2, and CeO_{2-x}).

SEM Bacteria Morphology Observation

To observe the SEM bacteria morphology, bacteria on the samples were fixed with

glutaraldehyde solution (2.5 vol%, 500 μL) overnight at 4 ℃after culturing at 37 °C for 24 h. Afterwards, the bacteria were further dehydrated in a series of ethanol solutions (30, 50, 75, 90, 95, and 100 v/v%) and ethanol-Hexamethyldisilazane mixture solution (2:1, 1:1, 1:2 and 0:1, volume ratio) for 10 min each. Finally, bacteria morphology was observed using a scanning electron microscope (SEM, S3400, HITACHI, Japan).

Cytocompatibility Evaluation

Cell Culture

Mouse osteoblasts cells (MC3T3-E1) (cells were kindly provided by Cell Bank of Chinese Academy of Sciences, Shanghai, China) were used to evaluate the cytocompatibility of Ti, Ce-BTC, CeO_2, and CeO_{2-x}. The cells were cultured with α-minimum essential medium containing 10% fetal bovine serum and 1% antimicrobial of penicillin and streptomycin under standard cell culture conditions (5% CO_2, 37 ℃and 100% humidity). The cell culture medium was refreshed every 3 days and the cells were sub-cultured when they reached 80–90% confluence.

Cell Proliferation and Morphology Observation

AlamarBlue assay was performed to evaluate cell proliferation. More specifically, MC3T3-E1 cells with the cell density of 5×10^4 cells/mL were introduced into a 24-well plate and cultured with various samples for 1, 4, and 7 days. At each time point, the culture medium was discarded and 0.5 mL of α-MEM with 10% (v/v) alamarBlue was introduced and cultured for another 2 h. Afterwards, the fluorescence intensity of the as-mentioned solution was examined by Cytation 5 Multi-Mode Reader (BioTek,

USA) with an excitation wavelength of 560 nm and an emission wavelength of 590 nm. For SEM morphology observation, the cells were fixed with glutaraldehyde solution (2.5%) overnight and dehydrated in accordance with the descriptions as mentioned in the section of SEM Bacteria Morphology Observation.

Cell Live/Dead Staining

A Live/Dead cell staining kit (Thermo Fisher Scientific Inc., USA) was used to assess the cytotoxicity of Ti, Ce-BTC, CeO_2, and CeO_{2-x}. Briefly, MC3T3-E1 cells with the cell density of 5×10^4 cells/mL were inoculated on Ti, Ce-BTC, CeO_2, and CeO_{2-x} and cultured for 4 days. After culturing for 4 days, the cell medium was discarded and the samples were rinsed with PBS. Then, 200 μL of PBS with propidium iodide (5 μM) and calcium-AM (2 μM) was introduced to each sample and incubated at 37 °C for 15 min. At last, the cells were rinsed with PBS twice and observed with a fluorescence microscope (Olympus, Japan).